Journal of the Optical Society of America B
OPTICAL PHYSICS

Mode analysis of second-harmonic generation in plasmonic nanostructures

GABRIEL D. BERNASCONI,* JÉRÉMY BUTET, AND OLIVIER J. F. MARTIN

Nanophotonics and Metrology Laboratory (NAM), Swiss Federal Institute of Technology Lausanne (EPFL), 1015, Lausanne, Switzerland
**Corresponding author: gabriel.bernasconi@epfl.ch*

Received 23 December 2015; revised 26 February 2016; accepted 27 February 2016; posted 29 February 2016 (Doc. ID 256355); published 30 March 2016

Using a surface integral equation approach based on the tangential Poggio–Miller–Chang–Harrington–Wu–Tsai formulation, we present a full wave analysis of the resonant modes of 3D plasmonic nanostructures. This method, combined with the evaluation of second-harmonic generation, is then used to obtain a better understanding of their nonlinear response. The second-harmonic generation associated with the fundamental dipolar modes of three distinct nanostructures (gold nanosphere, nanorod, and coupled nanoparticles) is computed in the same formalism and compared with the other computed modes, revealing the physical nature of the second-harmonic modes. The proposed approach provides a direct relationship between the fundamental and second-harmonic modes in complex plasmonic systems and paves the way for an optimal design of double resonant nanostructures with efficient nonlinear conversion. In particular, we show that the efficiency of second-harmonic generation can be dramatically increased when the modes with the appropriate symmetry are matched with the second-harmonic frequency.

OCIS codes: (030.4070) Modes; (260.5740) Resonance; (190.0190) Nonlinear optics; (250.5403) Plasmonics; (000.4430) Numerical approximation and analysis; (050.1755) Computational electromagnetic methods.

http://dx.doi.org/10.1364/JOSAB.33.000768

1. INTRODUCTION

Optical resonances in photonic nanostructures represent a vivid field of research, with emphasis on plasmonic nanostructures, where the extreme field enhancement and confinement, behind the classical diffraction limit [1–3], are promising for many applications such as biological sensing and optical signal processing down to the nanoscale [4–7]. Furthermore, the control of the resonant response of individual plasmonic and dielectric nanoparticles (including the resonance wavelength, the radiation pattern, and the resonance width, in both the linear and nonlinear regimes) is important for the design of metasurfaces that incorporate several subwavelength structures to produce an exotic behavior, such as a wavefront with controlled phase, for example [8,9]. Using the coupling and hybridization between different modes is a convenient method for tailoring and controlling all these properties [10–12].

In this context, it is crucial to understand the underlying mode properties of dielectric and plasmonic nanostructures. Indeed, the response of a resonant system to an external excitation can be understood as the projection of the excitation field onto its eigenmodes. The coupling strength between one given eigenmode and the excitation field depends on several parameters, including the symmetry, the polarization, and the frequency mismatch between the eigenfrequency and the frequency of the driving field. In the case of plasmonics, the knowledge of the modes can be used to obtain substantial near-field enhancement, absorption, and/or scattering at a specific wavelength. Several methods have been developed in order to obtain the electromagnetic resonances of a nanostructure. These methods can be separated into two main categories: those developed in the quasi-static [13–21] and dipolar [22] approximations and those using a full wave analysis method [23–26]. Each category includes several formulations, such as volume [27] and surface integral equations methods [23], direct application of the Green's tensor method [22,28], and direct expression of the electrostatic interaction between surface charges [14,16–19]. All these methods correspond to the derivation of an eigenvalue problem. However, it is important to note that, due to the presence of losses (both ohmic and radiative), the eigenfrequencies are complex and the eigenmodes are referred to as quasi-normal modes, in opposition to the normal modes observed in lossless cavities [24,26,29–36]. The completeness and orthogonality of the basis formed by the quasi-normal modes have been discussed in detail [29–31] and were proved for simple dielectric nanoparticles [37,38]. In a more general case, the quasi-normal modes orthogonality has been proven neglecting the spectral dispersion of the permittivity [34]. One of the main concerns about the

quasi-normal modes is that the associated fields diverge with the distance from the system due to the imaginary part of the eigenfrequency, making their normalization challenging [33]. It was recently proposed to use perfectly matched layer (PML) to bound the quasi-normal modes and to normalize them [34]. Such an issue is not problematic in the surface integral equation (SIE) method used here because only the scatterer's surface needs to be discretized and no external boundary conditions for the outgoing waves need to be imposed, with the radiation condition being directly fulfilled in this approach.

Since plasmonic systems are, in general, small in comparison with the incident wavelength, and because many applications rely mainly on the lowest order dipolar modes, methods developed in the quasi-static approximation are often adequate for understanding the underlying physical mechanisms in those systems. On the other hand, it is mandatory to go beyond this approximation when the nanostructures grow in size, with their dimensions becoming close to the wavelength of light. This is particularly true in nonlinear plasmonics, when the generated nonlinear signal has a wavelength shorter than the incident light [39]. In this case, retardation effects become non-negligible and the calculations must account for the field variations over the considered structure. This point is particularly important for one of the nonlinear optical processes, second-harmonic generation (SHG), which represents the focus of this paper and is forbidden in centrosymmetric media in the electric dipole approximation [40]. As a direct consequence, SHG from centrosymmetric nanoparticles, such as nanospheres, requires retardation effects and the excitation of high-order multipoles, like quadrupoles and octupoles [41–45].

Recently, mode matching between fundamental and second-harmonic modes in both the spatial and frequency domains has been demonstrated to yield a high nonlinear conversion [46–48]. Knowledge of the mode structure offers a useful tool for engineering the nonlinear properties. The simplest, but limited, method to characterize the modes of a given nanostructure is to study its response to plane wave illumination over a large wavelength range and to extract the mode information from the scattering or absorption peaks. Such a method is very easy to implement, because any numerical method suitable for scattering calculations can be used [49]; unfortunately, this method cannot provide complete information on the modes for the following two reasons. First, a plane wave interacts weakly with any mode having a small net dipolar moment (the so-called dark modes [50]). Second, even though those dark modes can be excited, they often overlap spectrally with broad dipolar modes; the resulting response is, in general, a superposition of several resonances and a clear identification of the modes is not straightforward. As a consequence, the evaluation of the scattering spectrum is not the best tool for the investigation of the eigenmodes, in particular when weakly radiative modes are involved.

In this article, we combine a full wave analysis of the eigenmodes for 3D plasmonic nanostructures based on the SIE method with the computation of surface SHG based on the same formalism [51]. In Section 3, the SHG associated with the fundamental dipolar modes is computed and compared with the high-order modes, revealing the quadrupolar nature of the second-harmonic mode for three distinct nanostructures, namely, a gold nanosphere, a nanorod, and coupled nanoparticles. In the final section, we discuss how the proposed approach provides the direct relationship between fundamental and second-harmonic modes in complex plasmonic systems and demonstrate that this method is very well suited for designing multiresonant nanostructures with efficient second-harmonic generation. It is worth noting that the method proposed in this article is very general and not limited to non-centrosymmetric nanostructures, as reported in the case of the effective nonlinear susceptibility method, for example [52,53].

2. NUMERICAL METHODS

A. Surface Integral Equation Formulation

The SIE allows the computation of the spatial distribution of the electric and the magnetic fields from fictitious currents defined solely on the surface of the scatterers. Starting from Maxwell's equations and using vector analysis theorems and the properties of the Green's function, two equations can be derived for each homogeneous domain (e.g., the scatterer and the background), one for each field: the electric field integral equation (EFIE) and the magnetic field integral equation (MFIE). They relate the excitation and the scattered electromagnetic fields to the electric surface currents $\mathbf{J}$ and the magnetic surface currents $\mathbf{M}$. The method of moment (MoM) [54] together with Rao–Wilton–Glisson (RWG) [55] basis functions and a triangular surface mesh are used to numerically solve those two equations. The electric and magnetic surface current densities of the domain n are expanded on the RWG basis functions building a triangular mesh approximating the boundary surface [56],

$$\mathbf{J}_n = \sum_u \alpha_u \mathbf{f}_u^n, \tag{1}$$

$$\mathbf{M}_n = \sum_u \beta_u \mathbf{f}_u^n, \tag{2}$$

where the summations occur on all the mesh edges; $\mathbf{f}_u^n$ is the RWG function of the edge u associated with the domain n. α_u and β_u are the unknown coefficients that need to be determined. Each integral equation becomes a linear matrix equation relating a vector (the equivalent surface currents) to the excitation field. The corresponding matrix depends on the nanostructure geometry and the properties of the domains (dielectric constant). The elements of the vectors $\mathbf{J}$ and $\mathbf{M}$ are associated with an edge of the mesh and a RWG function.

Although only the EFIE or the MFIE is sufficient to compute the fields in all the domains, a combination of the two equations into one matrix (implying the same solution for the EFIE and MFIE) is found to lead to more accurate numerical results [57–59]. In other words, in order to further increase the numerical accuracy, one forms a linear combination of the EFIE and MFIE. Furthermore, the integral equations for each domain are added together. This can be written as

$$\begin{bmatrix} \sum_n i\omega\mu_n \mathbf{D}^n & \sum_n \mathbf{K}^n \\ \sum_n \mathbf{K}^n & -\sum_n i\omega\epsilon_n \mathbf{D}^n \end{bmatrix} \cdot \begin{bmatrix} \{\alpha\} \\ \{\beta\} \end{bmatrix} = \sum_n \begin{bmatrix} \mathbf{q}^{(E),n} \\ \mathbf{q}^{(H),n} \end{bmatrix}, \tag{3}$$

where the following submatrices and vectors have been introduced:

$$D^n_{u,v} = \int_{\partial V^\Omega_n} \mathrm{d}S \mathbf{f}^n_u(\mathbf{r}) \cdot \int_{\partial V^\Omega_n} \mathrm{d}S' \overline{\mathbf{G}}_n(\mathbf{r},\mathbf{r}') \mathbf{f}^n_v(\mathbf{r}'), \quad (4)$$

$$K^n_{u,v} = \int_{\partial V^\Omega_n} \mathrm{d}S \mathbf{f}^n_u(\mathbf{r}) \cdot \int_{\partial V^\Omega_n} \mathrm{d}S' \left[\nabla' \times \overline{\mathbf{G}}_n(\mathbf{r},\mathbf{r}')\right] \cdot \mathbf{f}^n_v(\mathbf{r}'), \quad (5)$$

$$q^{(E),n}_u = \int_{\partial V^\Omega_n} \mathrm{d}S \mathbf{f}^n_u(\mathbf{r}) \cdot \mathbf{E}^{\mathrm{inc}}_n(\mathbf{r}), \quad (6)$$

$$q^{(H),n}_u = \int_{\partial V^\Omega_n} \mathrm{d}S \mathbf{f}^n_u(\mathbf{r}) \cdot \mathbf{H}^{\mathrm{inc}}_n(\mathbf{r}), \quad (7)$$

where $\overline{\mathbf{G}}_n(\mathbf{r},\mathbf{r}')$ is the dyadic Green's function, and $\mathbf{E}^{\mathrm{inc}}_n(\mathbf{r})$ and $\mathbf{H}^{\mathrm{inc}}_n(\mathbf{r})$ are the electric and magnetic incoming fields, respectively. Equation (3) shows the final linear system: the first and second subrows correspond to the EFIE (relating $\{\alpha\}$ and $\{\beta\}$ to $q^{(E),n}$) and MFIE (relating $\{\alpha\}$ and $\{\beta\}$ to $q^{(H),n}$), respectively.

At this step, it is worth saying a few words about the different SIE formulations. When constructing the EFIE and MFIE, one can consider either the tangential or the normal components of the fields at the domain surface. This leads to two distinct formulations denoted as T- for the formulations considering the tangential components of the fields and N- for those considering the normal components [60]. In the present work and on the basis of our previous studies on linear scattering and SHG, we use the T-PMCHWT [61–63] formulation, since it provides accurate results for plasmonic nanostructures [56,57]. Note that the mN-Müller formulation was used in a previous study of the modal decomposition for plasmonic systems [23].

B. Eigenmodes

In this section, we show how the scattering formulation presented in the previous section can be transformed into an eigenvalue problem. Equation (3) can be re-expressed in the simple form

$$\mathbf{S}(\omega)\boldsymbol{\psi} = \mathbf{q}, \quad (8)$$

where the frequency-dependent SIE matrix is denoted $\mathbf{S}(\omega)$. At a resonance frequency, oscillations can exist in the system without external driving forces. Let us seek a solution $\boldsymbol{\psi}_i$ for the system of Eqs. (8) without any external excitation ($\mathbf{q} = 0$). Rewriting Eq. (8) as the eigenvalue problem

$$\mathbf{S}(\omega)\boldsymbol{\psi}_i = \xi_i \boldsymbol{\psi}_i = \mathbf{0}, \quad (9)$$

where $\boldsymbol{\psi}_i$ and ξ_i are the eigenvectors and eigenvalues, respectively, it is possible to search for the angular frequencies ω where one of the eigenvalues ξ_i tends to zero. In this case, the eigenvector associated with the vanishing eigenvalue corresponds to a resonant mode of the structure. The same approach has already been used, for example in Refs. [22,23], to evaluate the eigenmodes of different plasmonic multimers. Since radiative and ohmic losses are present in plasmonic systems, both the resonant frequencies and the eigenvalues associated with the modes are complex. The complex angular frequency is defined as $\omega = \omega_r + i\omega_i$ with $\omega_i < 0$, where this choice of sign is dictated by the chosen temporal dependence $\exp(-i\omega t)$ used throughout. For convenience, the resonant wavelength is considered instead of the frequency in the following. The complex wavelength is defined as $\lambda = \lambda_r + i\lambda_i$ with $\lambda_i > 0$ since $\lambda = 2\pi c/\omega$, c being the speed of light. The eigenvalue ξ_i itself does not have a particular physical meaning, but the frequency associated with a vanishing eigenvalue corresponds to the resonance frequency of one mode of the considered nanostructure. In the following, the word "eigenvalue" refers to the norm of the complex quantity ξ_i. The complex character of ξ_i does not have a physical meaning here and we seek solutions of Eq. (9) for $\xi_i = 0$, implicitly meaning that $|\xi_i| \to 0$. In order to find all the eigenfrequencies associated with a given geometry, one can scan the entire complex frequency plane, but this represents a brute force inefficient approach. To avoid the computation of too many "useless" points in the complex plane, which is very time consuming and computationally inefficient, one can use the scattering spectrum of the studied structure to obtain prior knowledge of the spectral position of the eigenmodes, as illustrated in Fig. 1. This scattering spectrum can be obtained either by a plane wave excitation or by a suitable dipolar excitation in order to couple to both bright and dark modes. Indeed, at the wavelength for which the norm of the smallest eigenvalue tends to zero, the real part of the wavelength is closely related to the resonant wavelength and its imaginary part relates to the half width at half-maximum of the scattering peak, i.e., to the losses [Fig. 1(a)]. When only one resonance is present, the spectrum is a Lorentzian and the real part of the wavelength corresponds exactly to the resonant wavelength. From a practical point of view, we first extract the central wavelengths and widths of the different peaks from the scattering spectrum, and then use them as starting points for the scan of the complex frequency plane [Fig. 1(b)]. The eigenvalues of the SIE matrix are then computed around those points until a dip leading

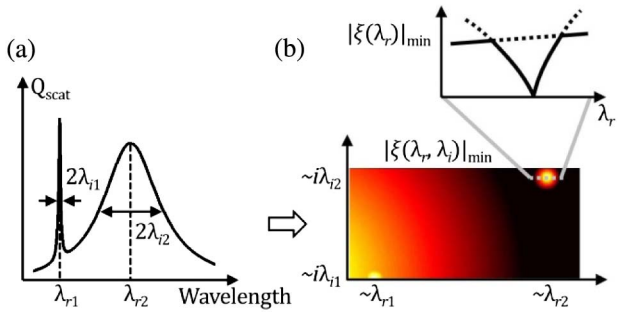

Fig. 1. (a) A typical example of the scattering spectrum used to find the approximate position and width of the maxima. In this case, the broad resonance would correspond to the dipolar mode and the narrow one to the quadrupolar dark mode. (b) Norm of the smallest eigenvalues in the complex plane as a function of the real and imaginary parts of the wavelength for a single sphere. Bright color corresponds to small values. The cut illustrates the emergence of the eigenvalue corresponding to the mode; see text.

to a minimum close to zero is found (typical residual value $\sim 10^{-9}$, depending on the number of edges). The advantage of obtaining the eigenmodes, in comparison with a mere analysis of the scattering, is that several modes can spectrally overlap at one frequency since plasmonic resonances are broad (typical quality factor $Q \sim 30$). For this reason, the near-field distribution associated with one scattering peak will not necessarily correspond exactly to that of a resonant eigenmode. This is particularly true for modes with low associated dipolar moments (dark modes) which are weakly coupled to far-field radiation. Figure 1 summarizes this approach.

Practically, only the smallest eigenvalue of the matrix was considered at each frequency. Indeed, since one looks for vanishing eigenvalues, considering only the smallest one does not lead to any loss of useful information. However, the subsequent smallest eigenvalues can also have a physical meaning in the case of degenerate modes, as discussed in Section 3. ARPACK routines ZNAUPD and ZNEUPD that apply the shift invert method were used to find the smallest eigenvalue of the matrix [64]. The 2D map of the smallest eigenvalue of the SIE matrix seems to follow a similar general behavior as does the absolute value of the permittivity, i.e., increasing both along the real and imaginary wavelengths. The fact of mapping only the smallest eigenvalue results in a sharp hole around the resonant frequency where the mapped smallest eigenvalue suddenly vanishes when it corresponds to the mode. This is visible in the cut in Fig. 1(b), where one observes the localized decrease of the smallest eigenvalue amplitude at the proximity of the resonant frequency.

Analytically, when an eigenvalue of a matrix is equal to zero, the matrix determinant is also zero. Another approach for finding the eigenfrequencies would be to compute the determinant of the SIE matrix for different complex frequencies instead of examining the smallest eigenvalue. Unfortunately, although the T-PMCHWT formulation is one of the most accurate SIE formulation for plasmonic nanostructures [56], the SIE matrix was found to lead to a very broad range of eigenvalues. This is expected, since the matrix is very ill-conditioned in this formulation [65]. The magnitude of the eigenvalues roughly ranges from 10^{-3} to 10^{3}, with a higher density at higher values. Furthermore, because the number of eigenvalues is equal to the number of edges in the mesh, commonly larger than a few hundred, computing the determinant for the SIE matrix appeared to be numerically challenging since it would quickly reach the highest or the lowest number storable by a computer, namely, 2^{1023} in double precision [e.g., for 200 edges and an average eigenvalue magnitude of 10^3:$(10^3)^{200} = 10^{600} > 2^{1023} \cong 10^{308}$]. In addition, the large number of eigenvalues with large magnitude does not allow for a smooth variation of the determinant, thus hiding the influence of a single vanishing eigenvalue. For those reasons, the approach described here, which limits the search to the smallest eigenvalue, seems the most suitable. Let us finally emphasize that the method described here and based on the SIE approach represents a full wave analysis and thus goes beyond the dipolar/quasi-static approximation. Furthermore, it is worth saying a few words about the mode amplitudes. The relative weights of the different modes have a physical meaning only when a specific excitation or state is projected on the eigenmodes basis: a mode does not have any intrinsic amplitude. However, as emphasized in the introduction, the projection of a plasmonic response on the eigenvector basis is a nontrivial problem since the fundamental question of the completeness and orthogonality of the quasi-normal modes basis is still under discussion.

C. Second-Harmonic Generation

The SIE method has been extended by Mäkitalo *et al.* to SHG from nanostructures driven by an incoming plane wave [66]. A similar approach is used here for the computation of SHG from the eigenmodes. It is well known that SHG is forbidden in the bulk of centrosymmetric media in the dipolar approximation and the main source of SHG is the surface nonlinear polarization oscillating at the second-harmonic frequency:

$$P_{\perp}(2\omega, \mathbf{r}^{+}) = \chi^{(2)}_{\perp\perp\perp} : E_{\perp}(\omega, \mathbf{r}^{-}) E_{\perp}(\omega, \mathbf{r}^{-}). \tag{10}$$

The + and − superscripts denote that the nonlinear polarization sheet is located just above the metal and the fundamental electric field is estimated just below the interface [67,68], respectively. The symbol $\perp$ denotes the component normal to the interface, and $\parallel$ denotes the tangential component. All components of the nonlinear susceptibility tensor, including the bulk contributions, can be implemented in this formalism. However, the $\chi^{(2)}_{\perp\perp\perp}$ component is known to be the strongest component of the nonlinear surface susceptibility for plasmonic nanostructures [69–71]. As a consequence, only this component will be considered in the following. The fundamental electric field close to the interface in domain n is related to the electric and magnetic surface current densities by [66]

$$\mathbf{M}_n = -\mathbf{E}_n \times \hat{\mathbf{n}}_n, \qquad \nabla_{\parallel} \cdot \mathbf{J}_n = -i\omega\epsilon_n \hat{\mathbf{n}}_n \cdot \mathbf{E}_n, \tag{11}$$

where $\hat{\mathbf{n}}_n$ is the outward normal vector on the boundary surface ∂V_n. In order to determine the second-harmonic electromagnetic field, the required set of boundary conditions, including the nonlinear polarization sheet standing at the interfaces, are used [66,72],

$$(\mathbf{E}^{\mathrm{SH}}(\mathbf{r}^{+}) - \mathbf{E}^{\mathrm{SH}}(\mathbf{r}^{-}))_{\parallel} = -\frac{1}{\epsilon'} \nabla_{\parallel} P_{\perp}, \tag{12}$$

$$(\mathbf{H}^{\mathrm{SH}}(\mathbf{r}^{+}) - \mathbf{H}^{\mathrm{SH}}(\mathbf{r}^{-}))_{\parallel} = 0, \tag{13}$$

where ϵ' is the so-called selvedge region permittivity [54]. As for the fundamental wave, the second-harmonic problem is solved using the MoM and expanding the equivalent second-harmonic surface densities on the RWG functions [55]. Using Galerkin's testing, a linear system of equations is derived from the boundary conditions in Eqs. (12) and (13). This linear system permits us to determine the electric surface current $\mathbf{J}_{\mathbf{SHG}}$ and the magnetic surface current $\mathbf{M}_{\mathbf{SHG}}$ oscillating at the second-harmonic frequency and then to compute the second-harmonic electromagnetic field associated with a given eigenmode.

3. RESULTS AND DISCUSSION

In the following, we illustrate the utilization of this approach by studying three distinct structures: a gold nanosphere, a dimer of gold nanospheres, and a gold nanorod. First, their eigenmodes are evaluated using the method described here and the fundamental (dipolar) modes are then used as sources of SHG.

Finally, the properties of the computed second-harmonic signals are compared with those of the higher order modes of the nanostructure. The aim of this comparison is to retrieve the multipolar nature of SHG in plasmonic nanostructures. All the nanostructures studied in this work are made of gold, the permittivity of which is obtained using the Drude model:

$$\epsilon(\omega) = \epsilon_\infty - \frac{\omega_p^2}{\omega^2 + i\omega\gamma}, \tag{14}$$

with $\epsilon_\infty = 9$, $\omega_p = 8.9$ eV, and $\gamma = 0.07$ eV. The first step is to obtain the resonance wavelengths for the structures and compute the corresponding charge distributions associated with the different eigenmodes. Indeed, losses result in a broadening and slight shift of the peak wavelength in the scattering spectrum, but our interest lies in the real part of the eigenfrequencies and in spatial distributions of the modes, quantities that are only slightly affected by losses. Furthermore, our analysis is only qualitative and we choose, without loss of generality, to ignore the losses in the Drude model. In addition, by neglecting the ohmic losses, the losses are limited to the radiative ones and will allow us to distinguish easily between bright and dark modes. In the case of dark modes, the research for the small eigenvalues is limited to the area close to the real line, i.e., for wavelengths with small imaginary parts [Fig. 1(b)]. All the nanostructures are considered in water (refractive index of the background $n = 1.33$), as it is the case in experiments performed on colloidal suspensions.

The method reported in this article is general, but we focus here on the design of double resonant nanostructures. As a consequence, we neglect the excitation channels involving cross coupling between different modes at the fundamental wavelength since their design for an efficient SHG is even more complicated. Indeed, in this case, the two fundamental modes must be resonant at the excitation wavelength. For example, using the dipolar mode as the source of the SHG, we neglect the channel $E_1 + E_2 \rightarrow E_1$, where the two terms on the left of the arrow refer to the nature of fundamental mode and the third term describes the second-harmonic emission mode and where subscript 1 stands for a dipolar mode and subscript 2 stands for a quadrupolar mode.

To validate our approach, modes were computed for a small sphere as well as for a small ellipsoid. The resulting resonance frequencies were then compared and found to be in agreement with the prediction of the Mie theory for the sphere and the electrostatic approximation for the ellipsoid [73]; see Tables 1 and 2. For convenience, the modes are presented in the following as surface charge distributions computed from the difference of the normal components of the electric field above and below the surface using Eq. (10) in [74].

Table 1. Resonance Wavelength in nm for a Ø 10 nm Gold Sphere in Vacuum

	Dipolar Mode	Quadrupolar Mode
Mie	$463.16 + i0.013$	$452.32 + i0.000$
SIE	$463.12 + i0.013$	$452.26 + i0.000$

Table 2. First Two Resonance Wavelengths in nm for a Gold Ellipsoid in Vacuum[a]

	Dipolar 1	Dipolar 2
Electrostatic	498.08	468.76
SIE	497.75	468.81

[a]The three semi axes are 5, 3.75, and 2.5 nm.

A. Gold Sphere

Analytically, the interaction between a sphere and an electromagnetic wave is described by the Mie theory. In this framework, the electric field $\mathbf{E}$ is expanded onto the vector spherical harmonic basis as

$$\mathbf{E} = \sum_{l,m} A_{l,m}\mathbf{M}_{l,m} + B_{l,m}\mathbf{N}_{l,m}, \tag{15}$$

where $\mathbf{M}_{l,m}$ and $\mathbf{N}_{l,m}$ are the vector spherical harmonics associated with the transverse electric (TE) modes and transverse magnetic (TM) modes, respectively, and are derived from the spherical harmonics of degree l and order m

$$Y_l^m(\theta, \varphi) = Ce^{im\varphi}P_l^m(\cos(\theta)), \tag{16}$$

where P_l^m is the associated Legendre polynomial, and C is a normalization constant [75]. The collective oscillations of the conduction electrons, corresponding to localized surface plasmon resonances, induce strong surface polarization charges and are then associated with the TM modes. Indeed, the presence of surface polarization charges requires the discontinuity of the normal component of the electric field at the nanoparticle surface. Physically, the degree l is associated with the angular momentum of the mode and corresponds graphically to the number of nodes (appearing as a circle) present on the sphere. The order m ranges from $-l$ to l ($2l + 1$ possible values) and corresponds to half the number of azimuthal nodes. Each spherical harmonic Y_l^m exhibits a different set of nodes and antinodes. Note that the mode energy depends only on the degree l and not on the order m [75].

For a given degree l, there are $2l + 1$ different modes with distinct charge distributions. Therefore, the method described in Section 2.B will not be *a priori* able to distinguish between the modes with the same degree l and different orders m, since the only free parameter in this model is the energy/wavelength. It is, however, still possible to retrieve the different modes, as explained in the next paragraph.

The modes obtained for a 40 nm spherical gold nanoparticle are shown in Fig. 2. The first, second, and third rows correspond to the dipolar ($l = 1$), quadrupolar ($l = 2$), and octupolar ($l = 3$) modes, respectively. At the first resonance wavelength ($\lambda = 504$ nm) corresponding to $l = 1$, three eigenvalues much smaller than the others are found and the three eigenvectors reveal three orthogonal dipoles (Fig. 2, first row). For $l = 2$ and $l = 3$, the number of distinguishably small eigenvalues is, respectively, 5 and 7, corresponding to $2l + 1$ as expected. However, the surface charge distributions associated with the eigenvectors are not associated with single spherical harmonic. From linear algebra it is known that any linear combination of eigenvectors sharing an eigenvalue is also an eigenvector, since a superposition of modes associated with one specific

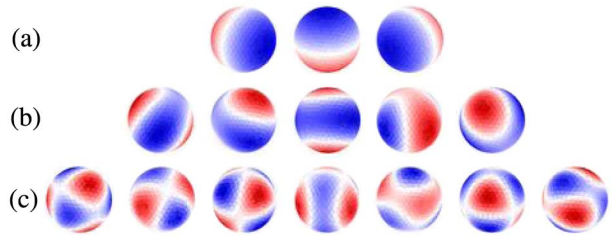

Fig. 2. First lower energy modes for a 40 nm gold sphere. The (a) first, (b) second, and (c) third rows correspond, respectively, to the dipolar mode ($l = 1$) at $\lambda = 504+i2.77$ nm, quadrupolar mode ($l = 2$) at $\lambda = 478+i0.02$ nm, and octupolar mode ($l = 3$) at $\lambda = 471+i0.08$ nm. For $l > 1$ it appears that the spherical harmonics are not retrieved.

eigenfrequency also exhibits divergent amplitude and corresponds to a resonant mode of the system. Furthermore, due to the mesh symmetry an eigenvector *a priori* displays the resonant mode in an arbitrary orientation, and nothing guarantees that this orientation is the same from one eigenvector to another, even if they are associated with the same degenerate eigenvalue. For example, the surface charge distributions obtained for the modes with $l = 2$ do not correspond to a single spherical harmonic but to a linear combination of spherical harmonics $Y^m_{l=2}$ of the same degree with different orders m and specific orientations (see Appendix A). Similar effects have been observed in Fig. 3 of [21]. The fact that dipoles are directly found for the modes of degree $l = 1$ but that a superposition of spherical harmonics is found for the quadrupolar ($l = 2$) and octupolar ($l = 3$) modes is surprising at first sight. However, a superposition of three dipoles with different orientations results in a dipole with a different orientation. This is not the case for quadrupolar (and higher order) modes due to the more complex spatial distribution of the charges associated with different order m.

In this framework, the mesh describing the nanoparticle surface plays an important role. Indeed, a curved surface is difficult to approximate with planar triangles. In order to check the influence of the mesh on the found eignemodes, the mesh reproducing the 40 nm nanosphere was tilted by a 45° angle. In this case, the two dipolar modes oriented perpendicularly to this rotation axis were also rotated with the same angle, following the asymmetry induced by the surface mesh (see Appendix B for a more detailed discussion). Let us emphasize that the previous considerations about degenerated eigenvalues and the influence of the mesh symmetry are less problematic when realistic structures (i.e., without specific symmetry) are considered.

Having confirmed with Mie theory the accuracy of the SIE method to compute the eigenmodes in the case of gold nanospheres, let us turn our attention to the main topic of this article, the SHG associated with these eigenmodes. Although the connection between fundamental and second-harmonic modes is now well-established for spherical nanoparticles [76–82], it is worth discussing it to benchmark the proposed approach for a better understanding of SHG in plasmonic nanostructures. In general, the incident fundamental wave is described by a

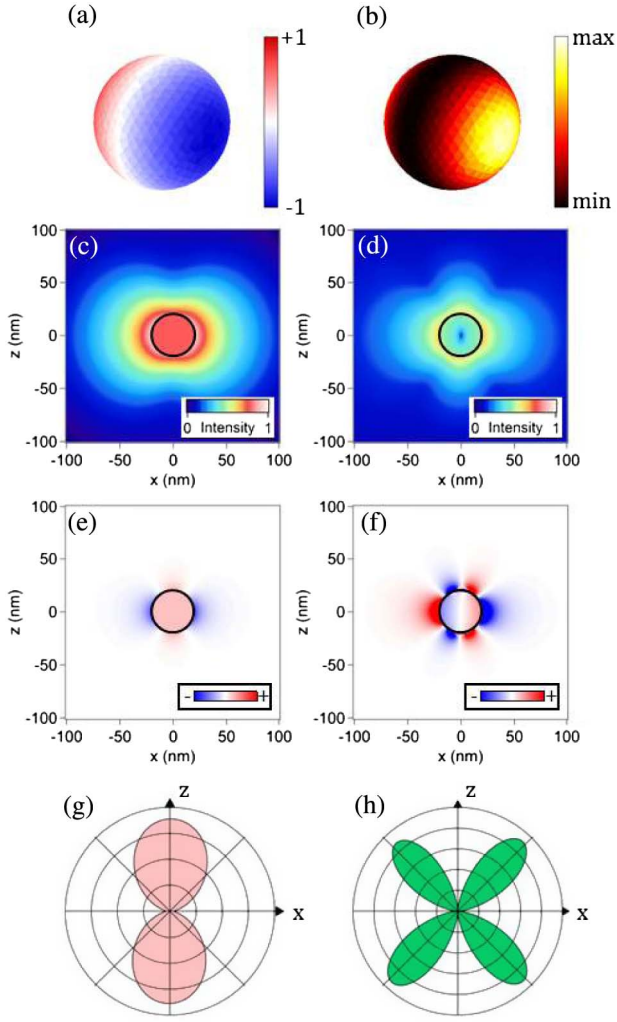

Fig. 3. Linear and second-harmonic response of a 40 nm gold nanosphere. (a) The charge distribution associated with the fundamental dipolar mode. (b) Nonlinear surface polarization associated with this mode computed using Eqs. (10) and (11). Near-field distributions of the (c) fundamental intensity and (e) real part of the x-component of the fundamental electric field. Near-field distribution of the (d) second-harmonic intensity and (f) real part of the x-component of the second-harmonic electric field. Far-field radiation patterns of the (g) fundamental mode and (h) second-harmonic signal.

linearly polarized plane wave propagating in the embedding medium. The expansion of plane wave polarized along the x-axis and propagating along the z-axis over the vector spherical harmonics basis involves only the terms with an order $m = \pm 1$, meaning that the set of excited fundamental modes is established by the symmetry of the driving field [73]. For this reason, we select the dipolar mode with its dipolar moment pointing along the x-axis as the fundamental mode [Fig. 3(a)]. The resonant wavelength of this mode is $\lambda = 504+i2.77$ nm. As discussed in Section 2, SHG arises from the surface of the plasmonic nanostructures due to the local centrosymmetry breaking. The corresponding nonlinear source, the surface nonlinear polarization, is computable using Eqs. (10) and (11), where the electric surface current $\mathbf{J}$ is given by the coefficients

α of the eigenvector associated with the fundamental mode [Fig. 3(b)]. In order to further emphasize the differences between the second-harmonic and fundamental modes, the corresponding near-field distributions of the intensity and of the real part of the x-component of the electric field associated with these two modes are shown in Fig. 3. The near-field distributions clearly reveal that the parity of the fundamental and second-harmonic modes is different. The fundamental mode corresponds to an odd (dipolar) mode, while the second-harmonic mode corresponds to an even (quadrupolar) mode. The multipolar nature of the SHG from spherical metallic structures has been extensively discussed in the past and is closely related to the centrosymmetry breaking induced by field retardation [43]. Here, the second-harmonic channel is $E_1 + E_1 \rightarrow E_2$. Indeed, the fundamental mode is an electric dipole, and the $E_1 + E_1 \rightarrow E_1$ mechanism, which would correspond to dipolar second-harmonic emission, is forbidden for centrosymmetric nano-objects. These results demonstrate that the proposed method is in agreement with previous experimental and theoretical investigations of the SHG from nanospheres [43]. It has been shown that deviations from a perfect sphere leads to a modification of the relative weight of the dipolar and quadrupolar contributions to the total second-harmonic emission [83]. Here, as observed in Fig. 3(h), the emission is perfectly quadrupolar, demonstrating that the mesh describing the sphere surface does not induce a dipolar second-harmonic emission resulting from any deviations from the perfectly symmetric case.

B. Gold Nanorod

Now, we turn our attention to nanostructures with lower symmetry, namely, gold nanorods. Plasmonic nanorods are important since they are the building blocks for optical antennas and several important metamolecules [84]. SHG from gold nanorods has been investigated, underlining the role played by the longitudinal plasmon resonance in the enhancement of the nonlinear response [85–87]. Here, we apply the same protocol as the one used previously for the study of the SHG from gold spheres.

The modes found for a 40 × 85 nm gold nanorod in water are shown in Fig. 4. The lower symmetry, in comparison with a spherical object, allows us to obtain well-defined quadrupolar modes in the longitudinal, respectively, transverse directions, at $\lambda = 503+i0.17$ nm, respectively, $\lambda = 491+i0.23$ nm. Note that, due to the asymmetry, the two quadrupolar modes do not have the same resonant wavelength as observed for the sphere; here the longitudinal mode has a lower energy than the transverse one. The transverse quadrupolar mode has a degeneracy of 2 and, as expected, two modes are actually found at the same wavelength (with identical charge distributions but with a 90° rotation around the rod axis, data not shown).

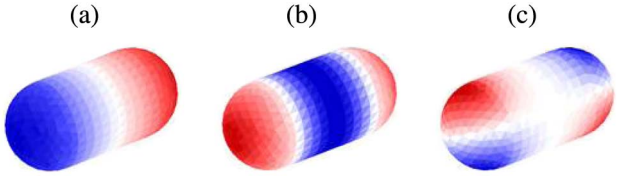

Fig. 4. Eigenmodes of a 40 × 85 nm gold nanorod: (a) the longitudinal dipolar mode at $\lambda = 647+i13.9$ nm, (b) the longitudinal quadrupolar mode at $\lambda = 503+i0.17$ nm, and (c) the transversal quadrupolar mode at $\lambda = 491+i0.23$ nm.

The longitudinal dipolar mode supported by a gold nanorod is coupled to an incoming plane wave polarized along its long axis and is responsible for the strong SHG from gold nanorods [85–87]. The nonlinear surface polarization associated with this mode is shown in Fig. 5(b), revealing that the nonlinear sources are mainly localized at the nanorod apexes. Despite a lower symmetry, nanorods are still centrosymmetric and SHG is still forbidden in the electric dipole approximation. As a consequence, the excitation channel involved here is also $E_1 + E_1 \rightarrow E_2$. The quadrupolar nature of the second-harmonic mode is confirmed by the computation of the electric

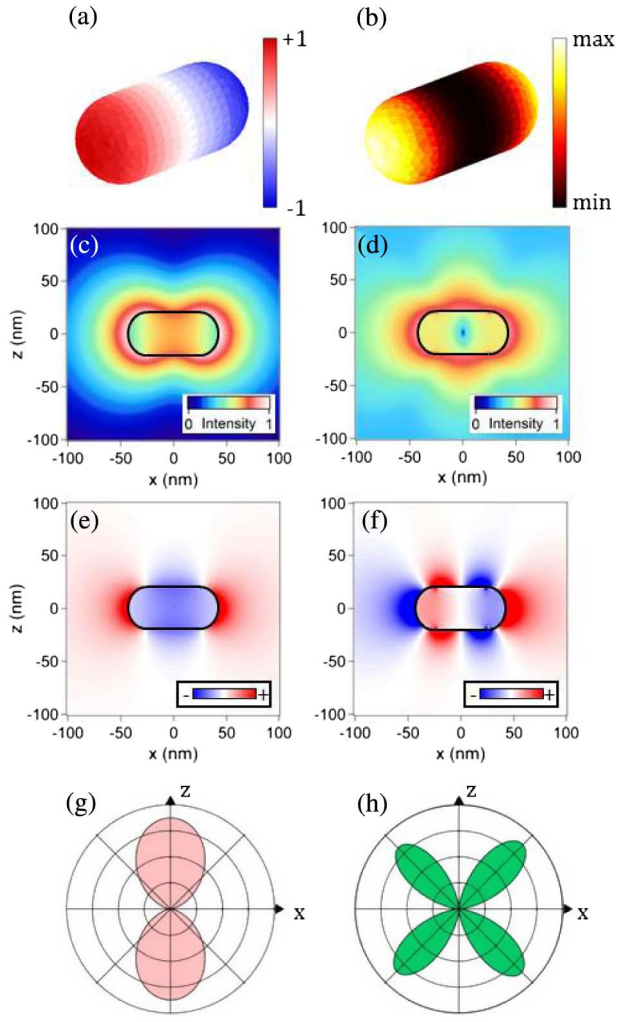

Fig. 5. Linear and second-harmonic response of a 40 × 85 nm gold nanorod. (a) Charge distributions associated with the fundamental dipolar mode. (b) Nonlinear surface polarization associated with this mode computed using Eqs. (10) and (11). Near-field distributions of the (c) fundamental intensity and (e) real part of the x-component of the fundamental electric field. Near-field distribution of the (d) second-harmonic intensity and (f) real part of the x-component of the second-harmonic electric field. Far-field radiation patterns of the (g) fundamental mode and (h) second-harmonic signals.

field in both the near-field and far-field regions (Fig. 5). Even more interesting is that the second-harmonic mode corresponds to the eigenmode shown in Fig. 4(b). These results demonstrate that the proposed method permits us to clearly identify the link between the fundamental mode and the second-harmonic mode. This point is important for the design of efficient plasmonic sources of second-harmonic light and of sensitive nonlinear plasmonic sensors.

C. Dimer of Gold Nanospheres

Finally, the case of coupled plasmonic nanostructures, the so-called nanoantennas, is considered. Previous studies on the SHG from plasmonic nanoantennas have revealed a singular behavior referred to as the silencing of SHG [88–90]. Indeed, despite strong fundamental near-field intensity in the gap, the SHG from plasmonic nanoantennas is not particularly enhanced. Although the nonlinear surface polarization is very large in this region, where the spheres are close to each other [see Fig. 7(b)], the second-harmonic sources standing at each side of the nanogap are out of phase, resulting in a far-field second-harmonic signal weaker than expected [88]. A dimer of two 40 nm gold spheres separated by a 5 nm gap is considered as an example of coupled nanostructures. Several modes are observed, as shown in Fig. 6.

To be able to resolve the high concentration of the charges in the nanogap due to Coulombian interaction, the mesh is specially refined in this region (smallest element size: 1 nm). The longitudinal dark mode shown in Fig. 6(c), corresponding to two facing dipoles, exhibits clear charge repulsion in the gap, contrary to the charge concentration associated with the bright dipolar mode [Fig. 6(a)]. Transverse modes are also observed, see Figs. 6(b) and 6(d), with vanishing eigenvalues of multiplicity equal to two (in each case both modes are rotated by 90° around the dimer axis with respect to each other, data not shown). These observations are now used for understanding the SHG from coupled nanoparticles. The nonlinear surface polarization associated with the fundamental dipolar mode, Fig. 7(a), is shown in Fig. 7(b) as well as the corresponding near-field and far-field distributions in Figs. 7(d), 7(f), and 7(h).

One can see that the nonlinear sources are extremely confined in the gap. As previously, the second-harmonic mode is an even mode (in the sense of parity) and the x-component of the second-harmonic field in the plane $x = 0$ vanishes. This observation is in agreement with our previous study on the SHG from coupled nanospheres [89]. However, even though it obeys to the right symmetry, the transverse mode shown in Fig. 6(b) does not correspond to the second-harmonic mode in the present case because its excitation requires retardation effects at the excitation stage [89] (i.e., at the fundamental wavelength).

This is not the case considering only a dipolar fundamental mode as done in the present eigenmode method. On the other hand, the design of efficient second-harmonic light generators must preferentially involve only one mode at the fundamental

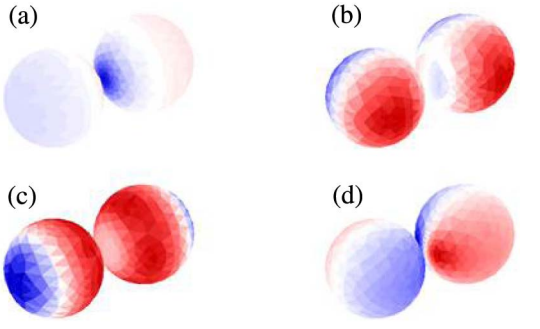

Fig. 6. Eigenmodes of a dimer of two 40 nm spheres with a gap of 5 nm. (a) Longitudinal dipolar mode at $\lambda = 551+i13.9$ nm. (b) Transversal dipolar mode at $\lambda = 498+i4.68$ nm. (c) Longitudinal dark mode at $\lambda = 489+i0.167$ nm. (d) Transverse dark mode at $\lambda = 517+i0.240$ nm.

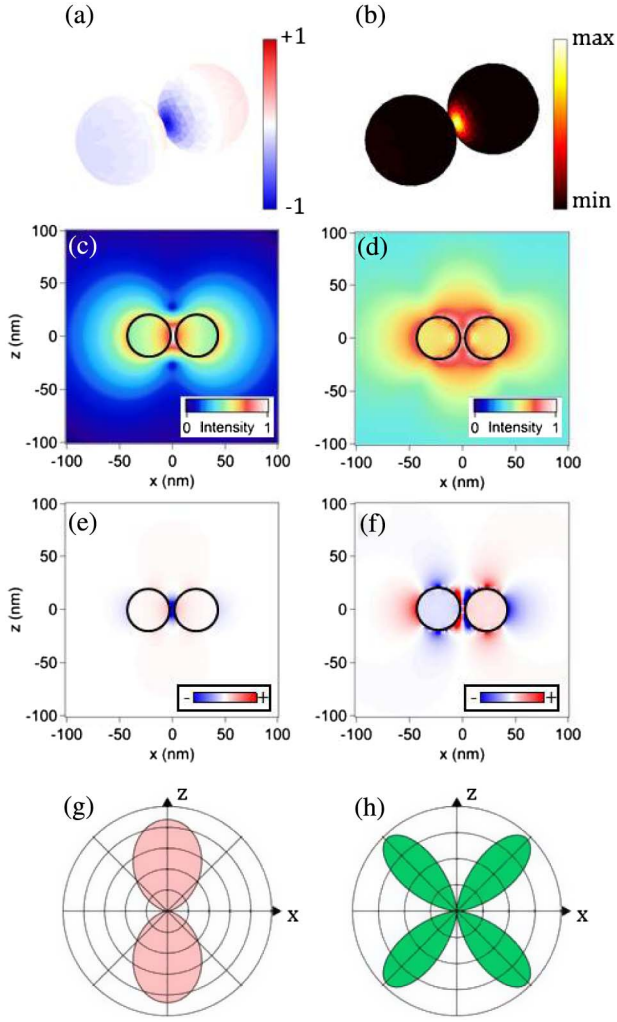

Fig. 7. Linear and second-harmonic responses of a dimer of two 40 nm gold nanospheres separated by a gap $g = 5$ nm. (a) The charge distribution associated with the fundamental dipolar mode. (b) Nonlinear surface polarization associated with this mode computed using Eqs. (10) and (11). Near-field distributions of the (c) fundamental intensity and (e) real part of the x-component of the fundamental electric field. Near-field distribution of the (d) second harmonic intensity and (f) real part of the x-component of the second-harmonic electric field. Far-field radiation patterns of the (g) fundamental mode and (h) second-harmonic signals.

excitation since modes are, in general, resonant at distinct wavelengths. In other words and using the previous notation, second-harmonic channels with $E_1 + E_1$ as the fundamental step should be preferred for a strong SHG. In this case, our method based on the eigenmodes allows us to determine the excited second-harmonic mode and then optimize the nanostructure geometry in order to tune its resonant wavelength close to the second-harmonic wavelength. This method is expected to be more efficient and effective than the plane wave excitation approach used so far.

D. Toward Engineering of the Second-Harmonic Mode

In this last section, we make a study of double resonant nanostructures and show that the nonlinear conversion can be dramatically improved by tuning the modes supported by these structures. In the quasi-static approximation, the only parameter that influences the resonance wavelengths for a given geometry and surrounding medium is the permittivity $\epsilon(\omega)$ of the particle [91]. For example, in the case of small spheres (i.e., in the quasi-static approximation), the resonant permittivities are given by $\epsilon(\omega) = -\epsilon_{bg}(l+1)/l$ with l a nonzero integer and ϵ_{bg} the background permittivity [73]. The dipolar and quadrupolar resonances are thus observed for $\epsilon_{\mathrm{dip}}(\omega) = -2\epsilon_{bg}$ and $\epsilon_{\mathrm{quad}}(\omega) = -1.5\epsilon_{bg}$, respectively. For larger nanostructures, retardation effects become non-negligible and the resonant frequencies depend on the nanoparticle size. In this study, the second-harmonic wavelength is fixed and corresponds to half the resonant wavelength of the considered fundamental mode. From Section 3.C, we know that SHG from the centrosymmetric structures investigated here is associated with a quadrupolar emission. However, as illustrated in Fig. 8(a) for the case of a sphere, the quadrupolar mode is usually not resonant at the second-harmonic wavelength. For this reason, we consider a fictitious material with varying permittivity at the second-harmonic frequency $\epsilon(2\omega)$, such that the quadrupolar mode is shifted to the second-harmonic wavelength, in order to boost the SHG [Fig. 8(a)]. We apply this idea to the three geometries studied in Section 3 and observe the variation of the second-harmonic signal intensity. The results are shown in Fig. 8(b). The important point is the very substantial increase of SHG intensity around the optimal permittivity, indicating that SHG can be improved by optimizing the mode matching. In the Drude model, the permittivity of gold at the three second-harmonic frequencies is positive (thus far from the optimal negative values needed). The ratio of the SHG intensity for the optimal $\epsilon(2\omega)$ and for the Drude permittivity (without loss) is $4.6 \cdot 10^4$ for the sphere, $1.1 \cdot 10^4$ for the nanorod, and $1.5 \cdot 10^3$ for the dimer. Note that for the sphere we obtain as optimal permittivity $\epsilon_{\mathrm{opt}} = -3$ instead of $\epsilon_{\mathrm{quad}} = -1.5\epsilon_{bg} = -2.65$. This small discrepancy is a consequence of the retardation effects due to the finite nanoparticle size and to the refractive index of the surrounding medium [92]. It is important to note that the absolute value of the SHG intensity enhancement for the three different nanostructures cannot be compared since the fundamental mode amplitudes are not normalized. Nevertheless, for each structure, the enhancement still describes how SHG can be enhanced by a suitable design of the plasmonic system.

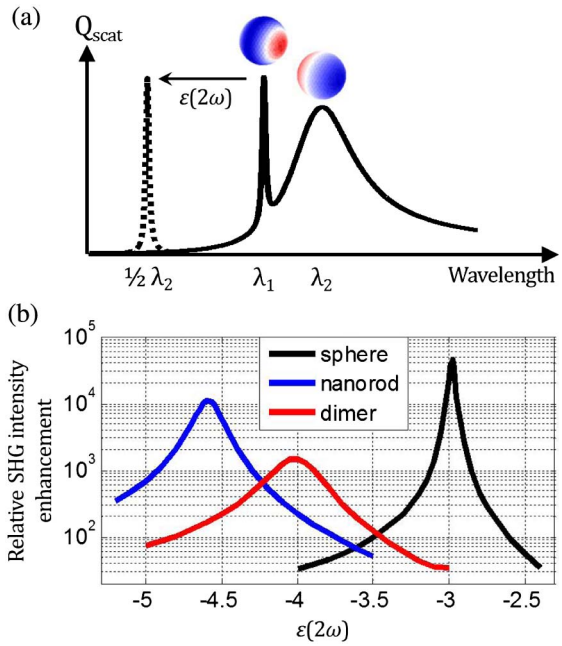

Fig. 8. (a) Scattering spectrum of a sphere. The quadrupolar mode can be shifted at half the wavelength of the dipolar mode by varying the nanostructure permittivity. (b) SHG intensity normalized to that obtained for the Drude model without losses at their respective second-harmonic frequencies (cf. Section 3) as a function of the second-harmonic permittivity $\epsilon(2\omega)$. Note that the Drude permittivity of gold at the second-harmonic frequencies is positive in the three cases and thus the second-harmonic plasmonic modes cannot be resonantly excited.

4. CONCLUSION

In summary, a new SIE method has been derived for the computation of the SHG directly from the fundamental eigenmodes. A gold nanosphere was considered as the first application, demonstrating that this method is able to accurately retrieve previously published results, especially the quadrupolar nature of the second-harmonic emission. SHG from a nanoparticle with a lower symmetry, a gold nanorod supporting longitudinal and transverse plasmon resonances, was then examined underlining that this approach can be extended to structures with low symmetry.

Finally, a coupled nanoparticle system, a gold nanodimer, has been investigated confirming the quadrupolar emission. These different examples illustrate the suitability of this approach for understanding the nonlinear response of complex plasmonic metamolecules. This approach will be instrumental for the design of efficient nonlinear sources of light at the nanoscale, as demonstrated in the last section, where a dramatic SHG is observed when modes with appropriate symmetry are matched with the second-harmonic frequency.

APPENDIX A: SPHERICAL HARMONIC SUPERPOSITION

Figure 9 shows two examples of linear combinations of spherical harmonics with degree $l = 2$. The resemblance (not

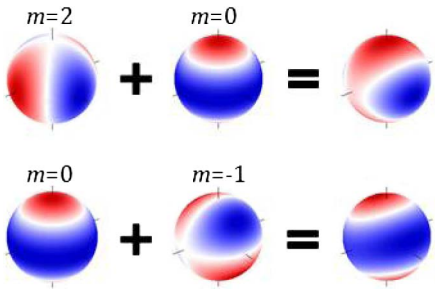

Fig. 9. Addition of a spherical harmonic of degree $l = 2$ with different order m. The similarity with the second row in Fig. 2 is obvious.

considering the orientations) with the five quadrupolar modes obtained for the sphere in Section 3.A is clearly observed.

APPENDIX B: INFLUENCE OF THE MESH SYMMETRY

To investigate the role of the mesh geometry on the eigenmodes of the sphere, an asymmetry, stronger than the inherent one, has been purposely introduced. This higher asymmetry results in a small splitting of the eigenfrequencies, previously degenerated, permitting us to partially retrieve the eigenmodes associated with single spherical harmonics. For example, when refining two opposite sides of the sphere (north and south poles) with triangles smaller than those used for the rest of the mesh, the quadrupolar modes ($l = 2$) appear with an eigenvalue degenerated only four times and the eigenmodes associated with the spherical harmonics $Y_{l=2}^{m=\pm1}$ are observed. Figure 10 shows four modes found with the modified mesh. Only four eigenvectors are shown because the next eigenvectors (associated with eigenvalues with increasing magnitude) were not physical solutions. We then assess that the degeneracy of the vanishing eigenvalue is only four. In this case, there is not a strong separation in the eigenvalue magnitudes, as observed with the original mesh.

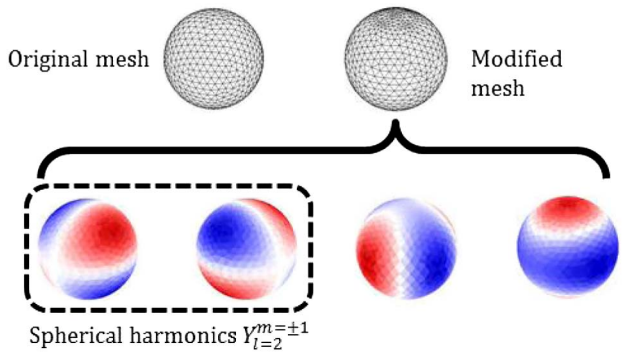

Fig. 10. Modified mesh with refined elements at two poles and associated eigenvectors. The degeneracy of the vanishing eigenvalue is reduced to 4 (instead of 5 with the original mesh). Two spherical harmonics are retrieved among the four eigenvectors. The eigenfrequency variation between the two meshes for this mode is less than 1 nm.

Funding. Swiss National Science Foundation (SNSF) (200020_153662).

REFERENCES

1. D. K. Gramotnev and S. I. Bozhevolnyi, "Plasmonics beyond the diffraction limit," Nat. Photonics **4**, 83–91 (2010).
2. J. A. Schuller, E. S. Barnard, W. S. Cai, Y. C. Jun, J. S. White, and M. L. Brongersma, "Plasmonics for extreme light concentration and manipulation," Nat. Mater. **9**, 193–204 (2010).
3. W. L. Barnes, A. Dereux, and T. W. Ebbesen, "Surface plasmon subwavelength optics," Nature **424**, 824–830 (2003).
4. K. A. Willets and R. P. Van Duyne, "Localized surface plasmon resonance spectroscopy and sensing," Annu. Rev. Anal. Chem. **58**, 267–297 (2007).
5. S. Lal, S. Link, and N. J. Halas, "Nano-optics from sensing to waveguiding," Nat. Photonics **1**, 641–648 (2007).
6. J. N. Anker, W. P. Hall, O. Lyandres, N. C. Shah, J. Zhao, and R. P. Van Duyne, "Biosensing with plasmonic nanosensors," Nat. Mater. **7**, 442–453 (2008).
7. K. F. MacDonald, Z. L. Samson, M. I. Stockman, and N. I. Zheludev, "Ultrafast active plasmonics," Nat. Photonics **3**, 55–58 (2009).
8. N. Yu and F. Capasso, "Flat optics with designer metasurfaces," Nat. Mater. **13**, 139–150 (2014).
9. P. Genevet and F. Capasso, "Holographic optical metasurfaces: a review of current progress," Rep. Prog. Phys. **78**, 024401 (2015).
10. E. Prodan, C. Radloff, N. J. Halas, and P. Nordlander, "A hybridization model for the plasmon response of complex nanostructures," Science **302**, 419–422 (2003).
11. N. J. Halas, S. Lal, W.-S. Chang, S. Link, and P. Nordlander, "Plasmons in strongly coupled metallic nanostructures," Chem. Rev. **111**, 3913–3961 (2011).
12. A. Lovera, B. Gallinet, P. Nordlander, and O. J. F. Martin, "Mechanisms of Fano resonances in coupled plasmonic systems," ACS Nano **7**, 4527–4536 (2013).
13. T. Sandu, "Eigenmode decomposition of the near-field enhancement in localized surface plasmon resonances of metallic nanoparticles," Plasmonics **8**, 391–402 (2013).
14. I. D. Mayergoyz, D. D. Fredkin, and Z. Zhenyu, "Electrostatic (plasmon) resonances in nanoparticles," Phys. Rev. B **72**, 155412 (2005).
15. G. Boudarham and M. Kociak, "Modal decompositions of the local electromagnetic density of states and spatially resolved electron energy loss probability in terms of geometric modes," Phys. Rev. B **85**, 245447 (2012).
16. D. E. Gómez, K. C. Vernon, and T. J. Davis, "Symmetry effects on the optical coupling between plasmonic nanoparticles with applications to hierarchical structures," Phys. Rev. B **81**, 075414 (2010).
17. C. Forestiere, L. Dal Negro, and G. Miano, "Theory of coupled plasmon modes and Fano-like resonances in subwavelength metal structures," Phys. Rev. B **88**, 155411 (2013).
18. K. C. Vernon, A. M. Funston, C. Novo, D. E. Gómez, P. Mulvaney, and T. J. Davis, "Influence of particle-substrate interaction on localized plasmon resonances," Nano Lett. **10**, 2080–2086 (2010).
19. T. J. Davis, K. C. Vernon, and D. E. Gómez, "Designing plasmonic systems using optical coupling between nanoparticles," Phys. Rev. B **79**, 155423 (2009).
20. W. Zhang and O. J. F. Martin, "A universal law for plasmon resonance shift in biosensing," ACS Photon. **2**, 144–150 (2015).
21. U. Hohenester and J. Krenn, "Surface plasmon resonance of single and coupled metallic nanoparticles: a boundary integral method approach," Phys. Rev. B **72**, 195429 (2005).
22. S. Dutta-Gupta and O. J. F. Martin, "Insight into the eigenmodes of plasmonic nanoclusters based on the Green's tensor method," J. Opt. Soc. Am. B **32**, 194–200 (2015).
23. J. Mäkitalo, M. Kauranen, and S. Suuriniemi, "Modes and resonances of plasmonic scatterers," Phys. Rev. B **89**, 165429 (2014).
24. Q. Bai, M. Perrin, C. Sauvan, J.-P. Hugonin, and P. Lalanne, "Efficient and intuitive method for the analysis of light scattering by a resonant nanostructure," Opt. Express **21**, 27371–27382 (2013).

25. M. S. Khajeahsani, A. Shahmansouri, M. J. Armand, and B. Rashidian, "Plasmonic resonance mode extraction based on the T-matrix method," J. Opt. Soc. Am. B **32**, 2333–2342 (2015).
26. J. R. D. Lasson, J. Mørk, and P. T. Kristensen, "Three-dimensional integral equation approach to light scattering, extinction cross sections, local density of states, and quasi-normal modes," J. Opt. Soc. Am. B **30**, 1996–2007 (2013).
27. H. Guo, B. Oswald, and P. Arbenz, "3-dimensional eigenmodal analysis of plasmonic nanostructures," Opt. Express **20**, 5481–5500 (2012).
28. G. Colas des Francs, J. Grandidier, S. Massenot, A. Bouhelier, J.-C. Weeber, and A. Dereux, "Integrated plasmonic waveguides: a mode solver based on density of states formulation," Phys. Rev. B **80**, 115419 (2009).
29. P. T. Leung, S. Y. Liu, and K. Young, "Completeness and orthogonality of quasi-normal modes in leaky optical cavities," Phys. Rev. A **49**, 3057–3067 (1994).
30. P. T. Leung, S. Y. Liu, S. S. Tong, and K. Young, "Time-independent perturbation theory for quasi-normal modes in leaky optical cavities," Phys. Rev. A **49**, 3068–3073 (1994).
31. P. T. Leung, S. Y. Liu, and K. Young, "Completeness and time-independent perturbation of the quasi-normal modes of an absorptive and leaky cavity," Phys. Rev. A **49**, 3982–3989 (1994).
32. E. S. C. Ching, P. T. Leung, A. Maassen van den Brink, W. M. Suen, S. S. Tong, and K. Young, "Quasi-normal-mode expansion for waves in open systems," Rev. Mod. Phys. **70**, 1545–1554 (1998).
33. P. T. Kristensen and S. Hughes, "Modes and modes volumes of leaky optical cavities and plasmonic nanoresonators," ACS Photon. **1**, 2–10 (2013).
34. C. Sauvan, J. P. Hugonin, I. S. Maksymov, and P. Lalanne, "Theory of the spontaneous optical emission of nanosize photonic and plasmon resonators," Phys. Rev. Lett. **110**, 237401 (2013).
35. R.-C. Ge, P. T. Kristensen, J. F. Young, and S. Hughes, "Quasi-normal mode approach to modelling light-emission and propagation in nanoplasmonics," New J. Phys. **16**, 113048 (2014).
36. P. T. Kristensen, C. V. Vlack, and S. Hughes, "Generalized effective mode volume for leaky optical cavities," Opt. Lett. **37**, 1649–1651 (2012).
37. P. T. Leung and K. M. Pang, "Completeness and time-independent perturbation of morphology-dependent resonances in dielectric spheres," J. Opt. Soc. Am. B **13**, 805–817 (1996).
38. K. M. Lee, P. T. Leung, and K. M. Pang, "Dyadic formulation of morphology-dependent resonances. I. Completeness relation," J. Opt. Soc. Am. B **16**, 1409–1417 (1999).
39. M. Kauranen and A. V. Zayats, "Nonlinear plasmonics," Nat. Photonics **6**, 737–748 (2012).
40. R. W. Boyd, *Nonlinear Optics* (Academic, 1992).
41. J. Butet, J. Duboisset, G. Bachelier, I. Russier-Antoine, E. Benichou, C. Jonin, and P.-F. Brevet, "Optical second harmonic generation of single metallic nanoparticles embedded in a homogeneous medium," Nano Lett. **10**, 1717–1721 (2010).
42. J. Butet, G. Bachelier, I. Russier-Antoine, C. Jonin, E. Benichou, and P. F. Brevet, "Interference between selected dipoles and octupoles in the optical second-harmonic generation from spherical gold nanoparticles," Phys. Rev. Lett. **105**, 077401 (2010).
43. J. I. Dadap, J. Shan, and T. F. Heinz, "Theory of optical second-harmonic generation from a sphere of centrosymmetric material: small-particle limit," J. Opt. Soc. Am. B **21**, 1328–1347 (2004).
44. I. Russier-Antoine, E. Benichou, G. Bachelier, C. Jonin, and P.-F. Brevet, "Multipolar contributions of the second harmonic generation from silver and gold," J. Phys. Chem. C **111**, 9044–9048 (2007).
45. E. C. Hao, G. C. Schatz, R. C. Johnson, and J. T. Hupp, "Hyper-Rayleigh scattering from silver nanoparticles," J. Chem. Phys. **117**, 5963–5966 (2002).
46. K. Thyagarajan, S. Rivier, A. Lovera, and O. J. F. Martin, "Enhanced second-harmonic generation from double resonant plasmonic antennae," Opt. Express **20**, 12860–12865 (2012).
47. M. Celebrano, X. Wu, M. Baselli, S. Großmann, P. Biagioni, A. Locatelli, C. De Angelis, G. Cerullo, R. Osellame, B. Hecht, L. Duò, F. Ciccacci, and M. Finazzi, "Mode matching in multiresonant plasmonic nanoantennas for enhanced second harmonic generation," Nat. Nanotech. **10**, 412–417 (2015).
48. K. Thyagarajan, J. Butet, and O. J. F. Martin, "Augmenting second harmonic generation using Fano resonances in plasmonic systems," Nano Lett. **13**, 1847–1851 (2013).
49. B. Gallinet, J. Butet, and O. J. F. Martin, "Numerical methods for nanophotonics: standard problems and future challenges," Laser Photon. Rev. **9**, 577–603 (2015).
50. B. Gallinet and O. J. F. Martin, "Influence of electromagnetic interactions on the line shape of plasmonic Fano resonances," ACS Nano **5**, 8999–9008 (2011).
51. J. Butet, B. Gallinet, K. Thyagarajan, and O. J. F. Martin, "Second-harmonic generation from periodic arrays of arbitrary shape plasmonic nanostructures: a surface integral approach," J. Opt. Soc. Am. B **30**, 2970–2979 (2013).
52. K. O'Brien, H. Suchowski, J. Rho, A. Salandrino, B. Kante, X. Yin, and X. Zhang, "Predicting nonlinear properties of metamaterials from the linear response," Nat. Mater. **14**, 379–383 (2015).
53. J. Butet and O. J. F. Martin, "Evaluation of the nonlinear response of plasmonic metasurfaces: Miller's rule, nonlinear effective susceptibility method, and full-wave computation," J. Opt. Soc. Am. B **33**, A8–A15 (2016).
54. R. F. Harrington, *Field Computation by Moment Methods*, Series on Electromagnetic Waves (IEEE, 1993).
55. S. Rao, D. Wilton, and A. Glisson, "Electromagnetic scattering by surfaces of arbitrary shape," IEEE Trans. Antennas. Propag. **30**, 409–418 (1982).
56. A. M. Kern and O. J. F. Martin, "Surface integral formulation for 3D simulations of plasmonic and high permittivity nanostructures," J. Opt. Soc. Am. A **26**, 732–740 (2009).
57. X. Q. Sheng, J. M. Jin, J. Song, W. C. Chew, and C. C. Lu, "Solution of combined-field integral equation using multilevel fast multipole algorithm for scattering by homogeneous bodies," IEEE Trans. Antennas Propag. **46**, 1718–1726 (1998).
58. P. Ylä-Oijala, "Application of a novel CFIE for electromagnetic scattering by dielectric objects," Microwave Opt. Technol. Lett. **35**, 3–5 (2002).
59. P. Ylä-Oijala and M. Taskinen, "Application of combined field Integral equation for electromagnetic scattering by dielectric and composite objects," IEEE Trans. Antennas Propag. **53**, 1168–1173 (2005).
60. C. Forestiere, G. Iadarola, G. Rubinacci, A. Tambourrino, L. D. Negro, and G. Miano, "Surface integral formulations for the design of plasmonic nanostructures," J. Opt. Soc. Am. A **29**, 2314–2326 (2012).
61. T.-K. Wu and L. L. Tsai, "Scattering from arbitrarily-shaped lossy dielectric bodies of revolution," Radio Sci. **12**, 709–718 (1977).
62. Y. Chang and R. F. Harrington, "A surface formulation for characteristic modes of material bodies," IEEE Trans. Antennas. Propag. **25**, 789–795 (1977).
63. A. J. Poggio and E. K. Miller, "Integral equations solutions of three dimensional scattering problems," in *Computer Techniques for Electromagnetics* (Pergamon, 1973).
64. R. B. Lehoucq, D. C. Sorensen, and C. Yang, *ARPACK Users' Guide: Solution of Large-Scale Eigenvalue Problems with Implicitly Restarted Arnoldi Methods* (Society for Industrial and Applied Mathematics, 1998).
65. A. Zhu and S. Gedney, "Comparison of the Müller and PMCHWT surface integral formulations for the locally corrected Nyström method," in *IEEE Antennas and Propagation Society International Symposium* (IEEE, 2004), Vol. **4**, pp. 3871–3874.
66. J. Mäkitalo, S. Suuriniemi, and M. Kauranen, "Boundary element method for surface nonlinear optics of nanoparticles," Opt. Express **19**, 23386–23399 (2011).
67. J. E. Sipe, V. C. Y. So, M. Fukui, and G. I. Stegeman, "Analysis of second-harmonic generation at metal surfaces," Phys. Rev. B **21**, 4389–4402 (1980).
68. V. Mizrahi and J. E. Sipe, "Phenomenological treatment of surface second-harmonic generation," J. Opt. Soc. Am. B **5**, 660–667 (1988).
69. F. X. Wang, F. J. Rodríguez, W. M. Albers, R. Ahorinta, J. E. Sipe, and M. Kauranen, "Surface and bulk contributions to the second-order nonlinear optical response of a gold film," Phys. Rev. B **80**, 233402 (2009).

70. D. Krause, C. W. Teplin, and C. T. Rogers, "Optical surface second harmonic measurements of isotropic thin-film metals: gold, silver, copper, aluminum, and tantalum," J. Appl. Phys. **96**, 3626–3634 (2004).
71. G. Bachelier, J. Butet, I. Russier-Antoine, C. Jonin, E. Benichou, and P.-F. Brevet, "Origin of optical second-harmonic generation in spherical gold nanoparticles: local surface and nonlocal bulk contributions," Phys. Rev. B **82**, 235403 (2010).
72. I. Hanninen, M. Taskinen, and J. Sarvas, "Singularity subtraction integral formulae for surface integral equations with RWG, rooftop and hybrid basis functions," Progress Electromagn. Res. **63**, 243–278 (2006).
73. C. F. Bohren and D. R. Huffman, *Absorption and Scattering of Light by Small Particles* (Wiley Interscience, 1983).
74. A. Ji, T. V. Raziman, J. Butet, R. P. Sharma, and O. J. F. Martin, "Optical forces and torques on realistic plasmonic nanostructures: a surface integral approach," Opt. Lett. **39**, 4699–4702 (2014).
75. G. B. Arfken and H. J. Weber, *Mathematical Methods for Physicists*, 6th ed. (Elsevier Academic, 2005).
76. Y. Pavlyukh and W. Hubner, "Nonlinear Mie scattering from spherical particles," Phys. Rev. B **70**, 245434 (2004).
77. B. Schürer, S. Wunderlich, C. Sauerbeck, U. Peschel, and W. Peukert, "Probing colloidal interfaces by angle-resolved second harmonic light scattering," Phys. Rev. B **82**, 241404 (2010).
78. D. Östling, P. Stampfli, and K. H. Benneman, "Theory of nonlinear optical properties of small metallic spheres," Z. Phys. D **28**, 169–175 (1993).
79. G. Gonella and H.-L. Dai, "Determination of adsorption geometry on spherical particles from nonlinear Mie theory analysis of surface second harmonic generation," Phys. Rev. B **84**, 121402(R) (2011).
80. J. Butet, I. Russier-Antoine, C. Jonin, N. Lascoux, E. Benichou, and P.-F. Brevet, "Nonlinear Mie theory for the second harmonic generation in metallic nanoshells," J. Opt. Soc. Am. B **29**, 2213–2221 (2012).
81. J. Butet, I. Russier-Antoine, C. Jonin, N. Lascoux, E. Benichou, and P.-F. Brevet, "Sensing with multipolar second harmonic generation from spherical metallic nanoparticles," Nano Lett. **12**, 1697–1701 (2012).
82. A. G. F. de Beer and S. Roke, "Nonlinear Mie theory for second-harmonic and sum-frequency scattering," Phys. Rev. B **79**, 155420 (2009).
83. G. Bachelier, I. Russier-Antoine, E. Benichou, C. Jonin, and P.-F. Brevet, "Multipolar second-harmonic generation in noble metal nanoparticles," J. Opt. Soc. Am. B **25**, 955–960 (2008).
84. H. Fischer and O. J. F. Martin, "Engineering the optical response of plasmonic nanoantennas," Opt. Express **16**, 9144–9154 (2008).
85. C. Hubert, L. Billot, P. M. Adam, R. Bachelot, P. Royer, J. Grand, D. Gindre, K. D. Dorkenoo, and A. Fort, "Role of surface plasmon in second harmonic generation from gold nanorods," Appl. Phys. Lett. **90**, 181105 (2007).
86. A. Singh, A. Lehoux, H. Remita, J. Zyss, and I. Ledoux-Rak, "Second harmonic response of gold nanorods: a strong enhancement with the aspect ratio," J. Phys. Chem. **4**, 3958–3961 (2013).
87. Y. El Harfouch, E. Benichou, F. Bertorelle, I. Russier-Antoine, C. Jonin, N. Lascoux, and P.-F. Brevet, "Hyper-Rayleigh scattering from gold nanorods," J. Phys. Chem. C **118**, 609–616 (2014).
88. J. Berthelot, G. Bachelier, M. Song, P. Rai, G. Colas des Francs, A. Dereux, and A. Bouhelier, "Silencing and enhancement of second-harmonic generation in optical gap antennas," Opt. Express **20**, 10498–10508 (2012).
89. J. Butet, S. Dutta-Gupta, and O. J. F. Martin, "Surface second-harmonic generation from coupled spherical plasmonic nanoparticles: eigenmode analysis and symmetry properties," Phys. Rev. B **89**, 245449 (2014).
90. A. Slablab, L. Le Xuan, M. Zielinski, Y. de Wilde, V. Jacques, D. Chauvat, and J.-F. Roch, "Second-harmonic generation from coupled plasmon modes in a single dimer of gold nanospheres," Opt. Express **20**, 220–227 (2012).
91. S. A. Maier, *Plasmonics: Fundamentals and Applications* (Springer, 2007).
92. H. Kuwata, H. Tamaru, K. Esumi, and K. Miyano, "Resonant light scattering from metal nanoparticles: practical analysis beyond Rayleigh approximation," Appl. Phys. Lett. **83**, 4625–4627 (2003).